Inorganic Chemistry

Article

pubs.acs.org/IC

Structural, Electrochemical, and Spectroscopic Investigation of Acetate Bridged Dinuclear Tetrakis-Schiff Base Macrocycles of Mn and Zn

Subhadeep Kal,[†] Alexander S. Filatov,[‡] and Peter H. Dinolfo*,[†]

[†]Department of Chemistry and Chemical Biology, Rensselaer Polytechnic Institute, 110 Eighth Street, Troy, New York 12180, United States

[‡]Department of Chemistry, University at Albany, State University of New York, Albany, New York 12222, United States

Supporting Information

ABSTRACT: The synthesis of $\mathbf{Mn_2LAc^+}$, $\mathbf{Zn_2LAc^+}$, and $\mathbf{H_4L^{2+}}$ is described, where **L** is a tetrakis-Schiff base macrocycle formed using 4-*tert*-butyl-2,6-diformylphenol and 2,2′-diamino-*N*-methyldiethylamine resulting in an N_6O_2 coordination environment. In $\mathbf{Mn_2LAc^+}$ and $\mathbf{Zn_2LAc^+}$, the two metal centers are bridged by an acetate ligand. $[Mn_2LAc](ClO_4)\cdot(DMF)_{0.5}$, $[Mn_2LAc](ClO_4)\cdot(ACN)_{0.5}$, and $[Zn_2LAc](PF_6)$ crystallized in the space group $P2_1/c$, with nearly identical unit-cell dimensions and geometric structures. Electrochemical analysis of $\mathbf{Zn_2LAc^+}$, and $\mathbf{H_4L^{2+}}$ by cyclic voltammetry (CV) revealed two irreversible anodic waves that were assigned to oxidations of the phenolate ligands. CVs of $\mathbf{Mn_2LAc^+}$ displayed two chemically reversible anodic waves corresponding to $Mn^{II/III}$ oxidations, followed by irreversible oxidations of the phenolate ligands. Interfacial electron transfer rates for the single electron oxidations from $\mathbf{Mn^{II}_2LAc^+}$ to $\mathbf{Mn^{II}Mn^{III}LAc^{2+}}$ to $\mathbf{Mn^{III}_2LAc^+}$ determined from digital simulation of the CVs were 0.6 and 1.1 × 10^{-3} cm s^{-1}, respectively. The sluggish interfacial electron transfer rates observed in electrochemical scans of $\mathbf{Mn_2LAc^+}$ are consistent with broken symmetry density functional theory electronic structure calculations (B3LYP/6-311G(2df)/6-311G(d,p)) that predict large structural rearrangements of the Mn coordination environment upon oxidation to Mn^{III} with associated Jahn−Teller distortions. Titration of $\mathbf{Mn_2LAc^+}$, $\mathbf{Zn_2LAc^+}$, and $\mathbf{H_4L^{2+}}$ with $NOPF_6$ in acetonitrile allowed for the isolation and spectroscopic examination of higher oxidations and were consistent with electrochemical assignments. The electrochemical and spectroscopic analysis of these complexes will aid in future studies involving electrocatalytic processes with related dinuclear macrocycles.

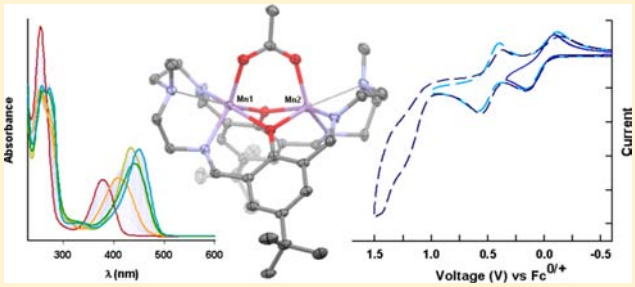

INTRODUCTION

Over the past several decades, there has been a significant research effort in the synthesis and characterization of biomimetic complexes resembling the oxygen-evolving complex (OEC) in photosystem II and dimanganese catalase enzymes, resulting in the creation many dimanganese, trimanganese, and tetramanganese coordination clusters.[1−4] We have recently become interested in dinuclear tetrakis-Schiff base-type complexes as potential electrocatalysts, because of their relative ease of synthetic tunability and their geometric arrangement of two adjacent coordination sites for substrate molecules bound to redox active metal centers.[5−10] In 1970, Robson showed that dinuclear tetrakis-Schiff base macrocycles could be self-assembled from 2,6-diformyl-4-methylphenol, 1,3-diaminopropane, and various first-row transition-metal dications, including Mn(II).[11,12] The resulting macrocycles provided an N_4O_2 coordination environment that placed the two metal centers ∼3 Å apart with adjacent coordination sites for counteranions or solvent molecules. Following this general procedure, numerous dimanganese tetrakis-Schiff base complexes have been reported.[13−24] In particular, Nagata and co-workers described a series of carboxylate-bridged dimanganese tetrakis-Schiff base macrocycles that employed a 2,2′-diamino-*N*-methyldiethylamine backbone, resulting in an N_6O_2 coordination environment for the two metal centers.[15−17] Electrochemical analysis of the structures showed a correlation between the redox potentials of the $Mn^{II/III}$ transitions and the substituents on the phenol ring and bridging carboxylate, but little other spectroscopic information of the compounds or characterization of higher oxidations were described. Subsequent studies showed promising catalase activity of these dimanganese complexes toward H_2O_2 disproportionation.[16,17] Given the reported catalase activity of these complexes and lack of subsequent catalytic studies, we were intrigued by their ability to act as water oxidation catalysts.

To provide a clearer understanding of the electrochemical and spectroscopic properties of these dimanganese tetrakis-Schiff base macrocycles, we synthesized $\mathbf{Mn_2LAc^+}$ and related analogues $\mathbf{Zn_2LAc^+}$ and $\mathbf{H_4L^{2+}}$ (Scheme 1) where the tetrakis-

Received: June 26, 2013
Published: November 21, 2013

Scheme 1. Synthetic Route to Mn_2LAc^+, Zn_2LAc^+, and H_4L^{2+}

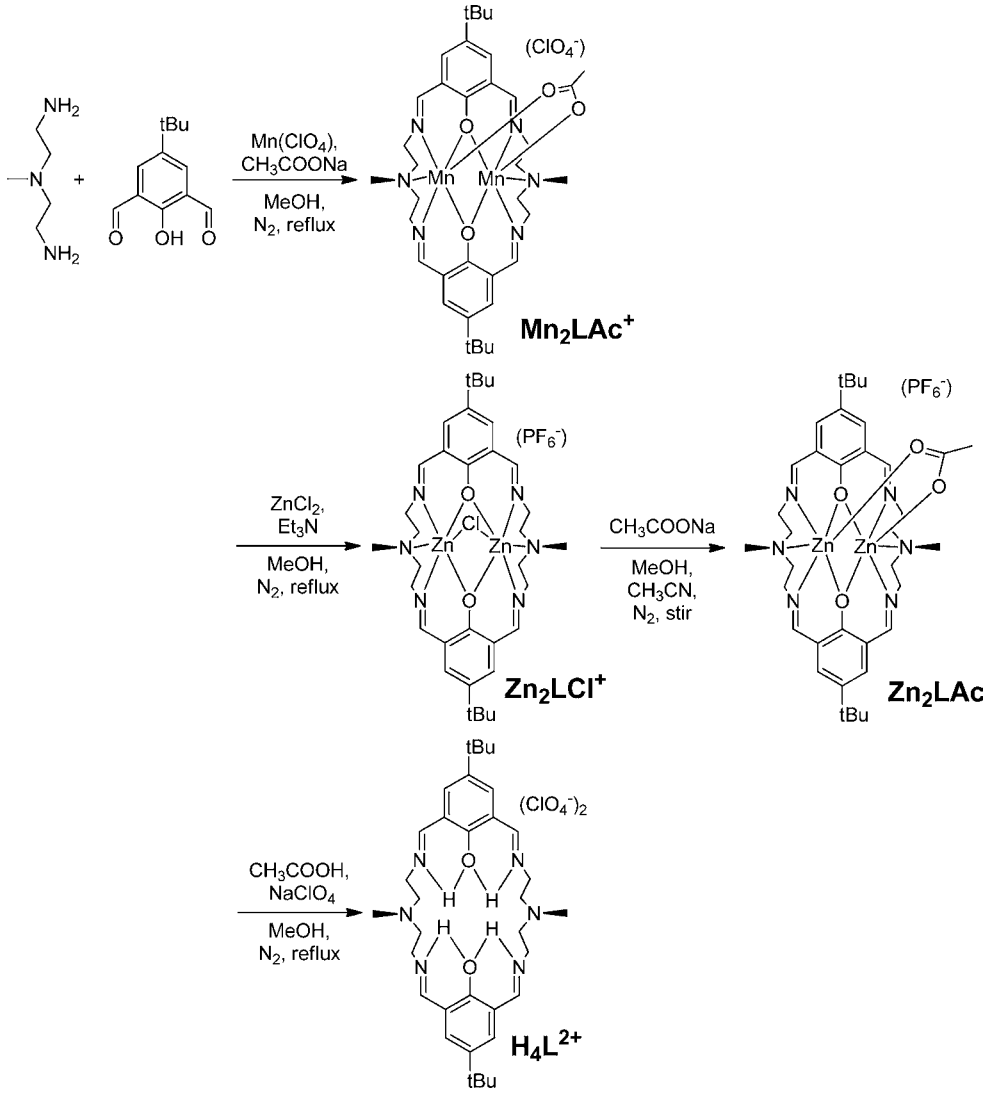

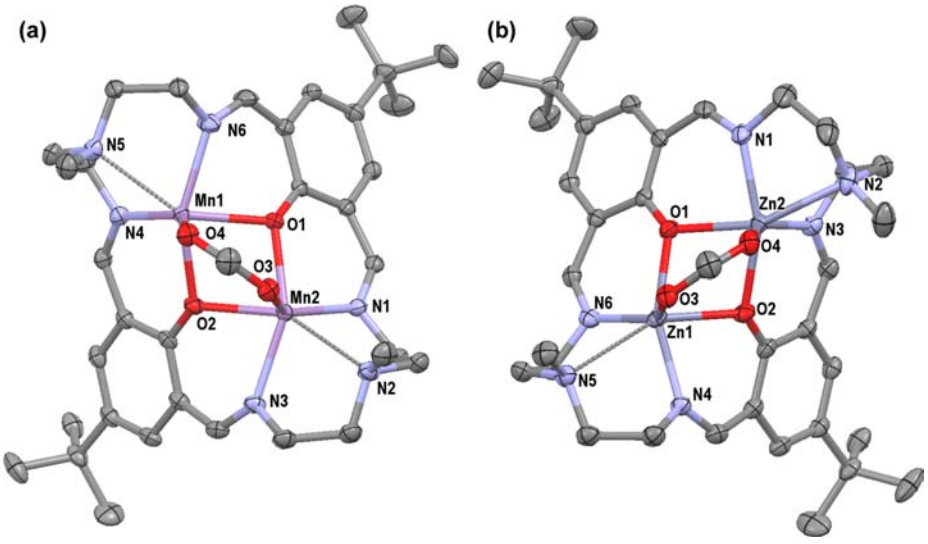

Figure 1. Top view ORTEP diagrams of (a) $[Mn_2LAc](ClO_4)\cdot(DMF)_{0.5}$ and (b) $[Zn_2LAc](PF_6)_5$ showing 50% probability thermal ellipsoids. Noncoordinating anion, hydrogen, and solvent atoms are omitted for clarity. The thin dashed lines represent elongated Mn−N and Zn−N bonds (>3 Å).

dx.doi.org/10.1021/ic401631e | *Inorg. Chem.* 2013, 52, 13963−13973

Table 1. Crystallographic Data and Structural Refinement Parameters for $[Mn_2LAc](C10_4)\cdot(DMF)_{0.5}$, $[Mn_2\ LAc](C10_4)\cdot(ACN)_{0.5}$, and $[Zh_2LAc](PF_6)$

	$[Mn_2LAc](ClO_4)\cdot(DMF)_{0.5}$	$[Mn_2LAc](ClO_4)\cdot(ACN)_{0.5}$	$[Zn_2LAc](PF_6)$
formula	$C_{75}H_{109}Cl_2Mn_4N_{13}O_{17}$	$C_{74}H_{105}Cl_2Mn_4N_{13}O_{16}$	$C_{36}H_{51}N_6O_4Zn_2F_6P$
fw	1755.41	1723.36	907.54
crystal system	monoclinic	monoclinic	monoclinic
space group	$P2_1/c$	$P\bar{1}$	$P2_1/c$
a [Å]	12.4348(14)	12.390(1)	12.290(2)
b [Å]	16.1580(19)	16.100(2)	16.324(3)
c [Å]	21.724(3)	21.389(3)	21.628(4)
α [deg]	90	90	90
β [deg]	106.501(2)	106.381(2)	106.093(3)
γ [deg]	90	90	90
V [Å^3]	4185.1(8)	4093.4(9)	4169.0(12)
Z	2	2	4
T [K]	100(2)	100(2)	100(2)
λ [Å]	0.71073	0.71073	0.71073
ρ (calcd, g/cm^3)	1.393	1.398	1.446
μ (mm^{-1})	0.725	0.739	1.26
reflections collected	9784	9607	9811
no. of observations $[I > 2\sigma(I)]$	8526	5884	7763
refln/param ratio	16.11	15.8	19.4
$R1^a$ $[I > 2\sigma(I)]$	0.0346	0.0513	0.0429
$wR2^b$ $[I > 2\sigma(I)]$	0. 0884	0.0963	0.1084
$R1^a$ (all data)	0.0407	0.1001	0.0559
$wR2^b$ (all data)	0. 0924	0.1110	0.1145
GOF^c on F^2	1.014	1.075	1.041

$^a R1 = (\sum||F_o| - |F_c||/\sum|F_o|$. $^b Rw(F_o^2) = [\sum[w(F_o^2 - F_c^2)^2/\sum wF_o^4]^{1/2}$. ^{c}GOF $= [\sum[w(F_o^2 - F_c^2)^2]/(N_{obs} - N_{params})]^{1/2}$.

Schiff base macrocyclic ligand (**L**) provides an octadentate N_6O_2 coordination site at the dinuclear core. $\mathbf{Mn_2LAc^+}$ and $\mathbf{Zn_2LAc^+}$ were structurally characterized by X-ray crystallography. The intermediates generated during oxidation of $\mathbf{Mn_2LAc^+}$, $\mathbf{Zn_2LAc^+}$, and $\mathbf{H_4L^{2+}}$ were characterized by cyclic voltammetry, electronic absorption, and infrared spectroscopy. These results were consistent with density functional theory (DFT) electronic structure calculations of $\mathbf{Zn_2LAc^+}$ and $\mathbf{Mn_2LAc^{n+}}$ (n = 1, 2, 3, and 4) and point to intricate electronic and structural changes involving both metal and ligand redox states. To the best of our knowledge, this is the first thorough spectroscopic and theoretical analysis of the higher oxidation states, generated chemically or electrochemically, of these or similar complexes.

RESULTS

Synthesis. The synthesis of symmetric dinuclear tetrakis-Schiff base complexes followed the method by Robson and Pilkington for $\mathbf{Mn_2LAc^+}$ and $\mathbf{Zn_2LAc^+}$, where **L** is the tetrakis-Schiff base ligand (Scheme 1). The method is based on a metal templated [2 + 2] macrocyclic condensation reaction of 4-*tert*-butyl-2,6-diformylphenol and 2,2′-diamino-*N*-methyldiethylamine with the transition-metal dications in refluxing methanol.[12] For $\mathbf{Mn_2LAc^+}$, acetate binding was achieved via the addition of sodium acetate to the reaction solution. $\mathbf{Zn_2LAc^+}$ was synthesized in a stepwise fashion with $ZnCl_2$ as the metal source yielding $\mathbf{Zn_2LCl^+}$. The bridging chloride was exchanged with the acetate anion by stirring with sodium acetate overnight in anhydrous acetonitrile (Scheme 1). $\mathbf{H_4L^{2+}}$ was synthesized by the proton-templated route of Dutta et al. with the addition of acetic acid to the reaction instead of the metal dication.[25] All compounds were confirmed by matrix-assisted laser desorption ionization (MALDI) or electron spin ionization (ESI) mass spectrometry, Fourier transform infrared (FTIR) spectroscopy, and elemental analysis. In addition, $\mathbf{Zn_2LAc^+}$, $\mathbf{Zn_2LCl^+}$, and $\mathbf{H_4L^{2+}}$ were characterized by ^{1}H NMR. Acetate binding in $\mathbf{Zn_2LAc^+}$ was confirmed by ^{1}H NMR with the appearance of a singlet at 2.3 ppm. In addition, two separate peaks for the N−CH_2−CH_2−NCH_3 protons were observed at 3.73 and 3.49 ppm, consistent with the nonsymmetric ligand structure around the dinuclear center observed with X-ray crystallography (vide infra).

X-ray Crystal Structures. The crystal structures of $[Mn_2LAc](ClO_4)\cdot(DMF)_{0.5}$ and $[Zn_2LAc](PF_6)_5$ are shown in Figure 1, as well as Figure S1 in the Supporting Information. Crystals of $\mathbf{Mn_2LAc^+}$ were obtained from two different solvent mixtures (acetonitrile and DMF), but the resulting unit cells and structures were nearly identical. The structure of $[Mn_2LAc](ClO_4)\cdot(ACN)_{0.5}$ is shown in Figure S2 in the Supporting Information. Attempts to crystallize $\mathbf{H_4L^{2+}}$ were unsuccessful. Table 1 includes crystallographic data and structural refinement parameters. Both $\mathbf{Mn_2LAc^+}$ and $\mathbf{Zn_2LAc^+}$ crystallize in the monoclinic space group $P2_1/c$, with very similar unit-cell dimensions, irrespective of counterions and solvent. Typical dinuclear tetrakis-Schiff base macrocycles with an N_4O_2 coordination environment yield coplanar structures with the metal centers in roughly square planar geometry.[13,20,26,27] The N_6O_2-type macrocycle afforded by the triamine backbone generates butterfly-like structures for $\mathbf{Mn_2LAc^+}$ and $\mathbf{Zn_2LAc^+}$ and forces the metal centers into highly distorted octahedral geometries. Similar phenomena have been observed with other dinuclear tetrakis-Schiff base macrocycles using a triamine backbone.[15−19,28,29] In this geometry, only one site per metal is available for external ligand coordination. For $\mathbf{Mn_2LAc^+}$ and $\mathbf{Zn_2LAc^+}$, these adjacent positions are occupied by a bridging acetate ion which hold the

dx.doi.org/10.1021/ic401631e | Inorg. Chem. 2013, 52, 13963−13973

Table 2. Selected Distances and Angles for Zn_2LAc^+ and Mn_2LAc^+ from the X-ray Crvstallographic Analysis

Bond Distances (Å)					
		$[Zn_2LAc](PF_6)$		$[Mn_2LAc](ClO_4)\cdot(DMF)_{0.5}$	$[Mn_2LAc](ClO_4)\cdot(ACN)_{0.5}$
	Zn1−Zn2	3.184	Mn1−Mn2	3.261	3.245
phenol	Zn1−O1	2.1352(18)	Mn1−O1	2.1989(11)	2.1918(19)
phenol	Zn1−O2	2.1083(17)	Mn1−O2	2.1841(11)	2.1754(18)
acetate	Zn1−O3	1.9893(17)	Mn1−O4	2.0995(11)	2.0921(19)
imine	Zn1−N4	2.099(2)	Mn1−N4	2.2013(13)	2.195(2)
amine	Zn1−N5	2.712(2)	Mn1−N5	2.60(2)	2.57(2)
imine	Zn1−N6	2.062(2)	Mn1−N6	2.1992(14)	2.179(13)
phenol	Zn2−O1	2.1108(17)	Mn2−O1	2.1896(11)	2.1830(17)
phenol	Zn2−O2	2.1126(17)	Mn2−O2	2.2085(11)	2.2024(18)
acetate	Zn2−O4	2.0329(18)	Mn2−O3	2.0949(12)	2.083(2)
imine	Zn2−N1	2.107(2)	Mn2−N1	2.2022(14)	2.193(3)
amine	Zn2−N2	2.400(2)	Mn2−N2	2.5512(14)	2.552(2)
imine	Zn2−N3	2.098(2)	Mn2−N3	2.2126(13)	2.199(2)

Bond Angles (deg)				
	$[Zn_2LAc](PF_6)$		$[Mn_2LAc](ClO_4)\cdot(DMF)_{0.5}$	$[Mn_2LAc](ClO_4)\cdot(ACN)_{0.5}$
O2−Zn1−O1	74.65(7)	O2−Mn1−O1	74.57(4)	74.58(7)
O1−Zn2−O2	75.07(7)	O1−Mn2−O2	74.27(4)	74.22(6)
Zn2−O1−Zn1	97.14(7)	Mn2−O1−Mn1	95.98(4)	95.74(7)
Zn1−O2−Zn2	97.92(7)	Mn1−O2−Mn2	95.86(4)	95.65(7)

metals 3.25 and 3.18 Å apart from each other, respectively. This type of ligand environment may be advantageous for catalytic applications, because it provides two adjacent coordination sites on the metals for substrate binding.

Table 2 contains selected bond lengths and angles for Mn_2LAc^+ and Zn_2LAc^+. The core geometries of both structures are quite similar, except that Zn_2LAc^+ is slightly smaller than that of Mn_2LAc^+, as expected based on the ionic radius of Zn^{2+}. The phenolic oxygens are symmetrically bonded to both metal centers with lengths averaging 2.12 Å and 2.19 Å for Zn−O and Mn−O respectively. Similarly, the imine-metal bond distances are symmetric for both structures, averaging 2.09 Å for Zn−N and 2.20 Å for Mn−N. In all structures, the amino-metal bond distances are significantly longer than those of the imine-metal, suggesting that these may be weak interactions. Some asymmetry exists in the Zn_2LAc^+ core structure as evident in the amino N−Zn bonds at 2.40 and 2.71 Å (the longer bond is shown as a dotted line in Figure S1 in the Supporting Information). In Mn_2LAc^+, the there is less structural asymmetry with the amino Mn−N bonds ranging from 2.55 Å to 2.60 Å.

Magnetic Susceptibility. The molar magnetic susceptibility of Mn_2LAc^+ in the solid state was measured by Gouy's method at room temperature . The μ_{eff} value obtained was 7.76 μ_B, which is lower than the expected value for an ferromagnetically coupled high spin $(Mn^{II})_2$ system (S = 10/2). This suggests a weak antiferromagnetic interaction between the Mn^{II} centers in Mn_2LAc^+. This is further supported by the DFT electronic structure calculations of Mn_2LAc^{n+} (n = 1, 2, 3, and 4) (vide infra). Similar weak antiferromagnetic interactions between Mn^{2+} ions have been observed for tetrakis-Schiff base macrocycles with N_6O_2 and N_4O_2 coordination environments.[13,18−23] It has been theorized that the weak antiferromagnetic coupling in the di-Mn^{2+} is a result of the relatively large ion size and longer bond distances, in comparison to other first-row transition-metal dications such as Fe^{2+}, Co^{2+}, Ni^{2+}, and Cu^{2+}, where the coupling increases as the ion size decreases.[21]

Electrochemistry. The electrochemistry of Mn_2LAc^+, Zn_2LAc^+, and H_4L^{2+} were examined by cyclic voltammetry (CV) and differential pulse voltammetry (DPV) in anhydrous dichloromethane (DCM) and acetonitrile (ACN). Representative CV and DPV scans for Mn_2LAc^+, Zn_2LAc^+, and H_4L^{2+} are shown in Figure 2, and the electrochemical data are compiled in Table 3. All potentials are referenced versus ferrocene/ferrocenium ($Fc^{0/+}$). By comparing the electrochemistry of Mn_2LAc^+, Zn_2LAc^+, and H_4L^{2+}, we were able to identify the redox couple responsible for each of the oxidations.

Cyclic voltammograms of Zn_2LAc^+ in anhydrous DCM (Figure 2d) showed two irreversible oxidation waves within the electrochemical solvent window at $E_{1/2}$ = 1.06 (peak III) and 1.22 V vs $Fc^{0/+}$ (peak IV). Similarly, cyclic voltammograms of H_4L^{2+} in anhydrous DCM (Figure 2e) also displayed two irreversible oxidation waves at $E_{1/2}$ = 0.89 (peak III) and 1.26 V vs $Fc^{0/+}$ (peak IV). Since the central Zn atoms are redox inactive within the experimental conditions, we can consider the above oxidations to be ligand-centered, specifically to the oxidation of phenolate moieties to corresponding phenoxyl radicals.[30,31] Salen-type complexes are known to generate phenoxyl radicals by oxidation of the phenolate moieties.[28,30−36]

CVs of Mn_2LAc^+ in anhydrous ACN are presented in Figure 2b. Two quasi-reversible oxidation processes are detected at $E_{1/2}$ = 0.03 and $E_{1/2}$ = 0.48 V vs $Fc^{0/+}$ (waves I and II, respectively). Comparison of the voltammetric and chronoamperometric responses of these waves at a glassy carbon microelectrode confirm these are single electron processes (n = 1) and yield a diffusion coefficient of 8.7 × 10^{-6} cm^2/s.[37] These electrochemical waves are consistent with those reported by Ikawa et al. for a similar complex[15] and are assigned as the sequential single electron oxidations of $Mn^{II}_2LAc^+$ to $Mn^{II}Mn^{III}LAc^{2+}$ and then $Mn^{III}_2LAc^{3+}$.

Scanning further to more-positive potentials reveals two more irreversible oxidations at 1.36 and 1.57 V vs $Fc^{0/+}$ (waves III and IV, respectively). Oxidative wave III is also discernible in anhydrous DCM (Figure 2c), but unfortunately the fourth

dx.doi.org/10.1021/ic401631e | Inorg. Chem. 2013, 52, 13963−13973

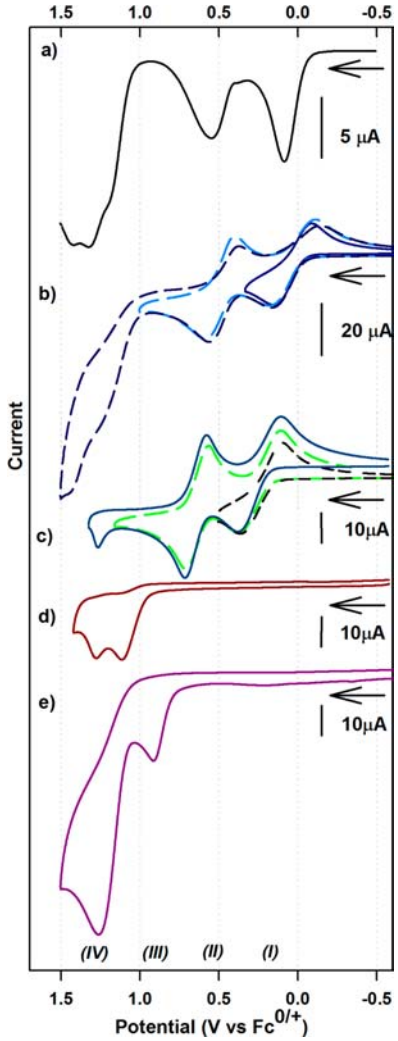

Figure 2. (a) Differential pulse voltammetry (DPV) scan of $\mathbf{Mn_2LAc^+}$ (1 mM) in ACN. (b) Cyclic voltammograms of $\mathbf{Mn_2LAc^+}$ (1 mM) in ACN. (c) Cyclic voltammograms of $\mathbf{Mn_2LAc^+}$ (1 mM) in DCM. (d) Cyclic voltammogram of $\mathbf{Zn_2LAc^+}$ (1 mM) in DCM. (e) Cyclic voltammogram of $\mathbf{H_4LAc^{2+}}$ (1 mM) in DCM. All cyclic voltammetry is performed at 298 K with $TBAPF_6$ supporting electrolyte at ν = 100 mV/s, glassy carbon working electrode, and platinum wire counter electrode. Arrows indicate the initial scan direction.

oxidation (Peak IV) is not observable within the electrochemical window of the solvent. Comparing the electrochemistry of $\mathbf{Mn_2LAc^+}$ (Figure 2c) with $\mathbf{Zn_2LAc^+}$ and $\mathbf{H_4L^{2+}}$ in anhydrous DCM, we observed a close overlap of peak III at ~1.26 V vs $Fc^{0/+}$. Such close agreement of this wave in the voltammograms for $\mathbf{Mn_2LAc^+}$ and $\mathbf{Zn_2LAc^+}$ suggests the origins of peaks III and IV to be oxidation of the phenolate moieties to phenoxyl radicals, although oxidation of the Mn centers to Mn^{IV} cannot be ruled out at this point. The higher charge density of the $Mn^{III}{}_2$ core in $\mathbf{Mn^{III}_2LAc^{3+}}$, compared to $\mathbf{Zn_2LAc^+}$, shifts the phenolate oxidations to a slightly higher potential. Similar manganese(III)-phenoxyl radical species in salen-type complexes have been reported previously.[31,34]

The relatively large potential difference between the $Mn^{II/III}$ redox transitions (waves I and II) for $\mathbf{Mn_2LAc^+}$ (ΔE_{II-I} = 450 mV) can be attributed in part to the strong electronic coupling between the two Mn centers as a result of their close proximity in the N_6O_2 core. For $\mathbf{Mn_2LAc^+}$, the equilibrium constant (K_c)

Table 3. Electrochemical Data for $\mathbf{Mn_2LAc^+}$, $\mathbf{Zn_2LAc^+}$, and $\mathbf{H_4LAc^{2+}}$ (V vs. $Fc^{0/+}$)

		Redox Process			
compound	solvent	I	II	III	IV
$\mathbf{H_4LAc^{2+}}$					
$E_{1/2}$ (V)	DCM			0.89[b]	1.26[b]
$\mathbf{Zn_2LAc^+}$					
$E_{1/2}$ (V)	DCM			1.06[b]	1.22[b]
$\mathbf{Mn_2LAc^+}$					
$E_{1/2}$ (V)	DCM	0.21	0.64	1.23[b,c]	
ΔE_p (mV)[d]	DCM	270	150		
$k°$ ($\times 10^{-3}$ cm/s)[e]	DCM	0.4	1.0		
$\mathbf{Mn_2LAc^+}$					
$E_{1/2}$ (V)	ACN	0.03	0.48	1.23[c]	1.44[c]
ΔE_p (mV)[d]	ACN	280	190		
$k°$ ($\times 10^{-3}$ cm/s)[e]	ACN	0.6	1.1	66	75

[a]Data obtained in dichloromethane (DCM) or acetonitrile (ACN) with 0.1 M $TBAPF_6$ as supporting electrolyte, using a glassy carbon working electrode, platinum wire counter electrode, and silver wire pseudo-reference electrode. [b]Irreversible oxidation wave. [c]Overlapping waves. [d]Anodic−cathodic peak spliting at 100 mV/s. [e]Interfacial electron transfer rate constant obtained from digital simulation of cyclic voltammograms.

for the comproportionation reaction can be calculated from eq 1.[38]

$$K_c = \frac{[(Mn^{III})(Mn^{III})L]^2}{[Mn^{II}_2L][Mn^{III}_2L]} = \exp\left[\frac{(E_2 - E_1)F}{RT}\right] \quad (1)$$

For $\mathbf{Mn_2LAc^+}$, the calculated K_c values of 5.8×10^6 in DCM and 4.0×10^7 in ACN suggest strong electronic interaction between the Mn centers. Such high K_c values are comparable with those reported for mixed-valence species with strong electronic coupling between metal redox centers spanned by rigid spacers.[39−42]

Redox processes I and II for $\mathbf{Mn_2LAc^+}$ show a significant increase in peak splitting at higher scan rates as shown in Figure 3. This type of deviation from ideal voltammetry indicates slow heterogeneous electron transfer and high reorganizational energies associated with these redox transformations.[43,44]

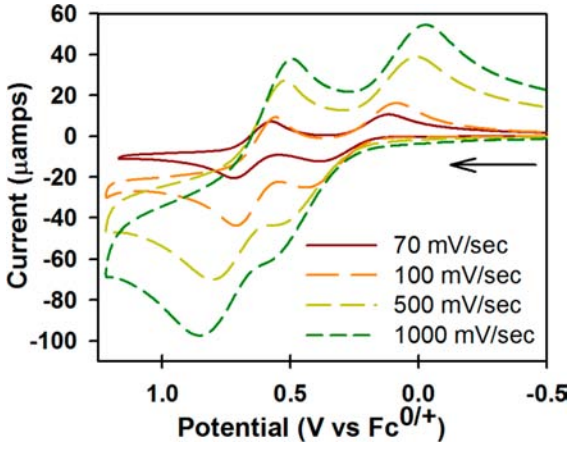

Figure 3. Cyclic voltammograms of $\mathbf{Mn_2LAc^+}$ (1 mM) in anhydrous DCM at scan rates of 70 mV/s (dark red), 100 mV/s (orange), 500 mV/s (green), and 1000 mV/s (dark green) using a glassy carbon working electrode. The arrow indicates the initial scan direction.

dx.doi.org/10.1021/ic401631e | Inorg. Chem. 2013, 52, 13963−13973

Digital simulation of the cyclic voltammograms in Figures 2 and 3 allowed us to extract the interfacial electron transfer rate constants ($k°$) for these electrode processes (see Table 3). Simulated CVs at various scan rates are shown in Figure S3 in the Supporting Information. The relatively slow values of $k°$ are consistent with the assignment of these waves as sequential oxidations of Mn^{II} centers, as the resulting Mn^{III} would cause significant geometry changes of the Mn-phenoxo core associated with a Jahn–Teller distortion.

Electronic Absorption Spectroscopy. The ground-state electronic absorption spectra of $\mathbf{Mn_2LAc^+}$, $\mathbf{Zn_2LAc^+}$, and $\mathbf{H_4L^{2+}}$ are shown in Figure 4. All three tetrakis-Schiff base macrocycles exhibit three primary absorbance bands in the UV–vis region at ~220, 250, and 360–440 nm. The close similarity of the spectra for these complexes suggests that the optical transitions are localized on the ligand framework. The lack of other absorption bands in the visible region is consistent with the absence of d–d transitions for the spectroscopically silent Zn^{II} (d^{10}) and Mn^{II} (high spin d^5) metal centers. The intense absorption bands around 250–260 nm and 215–220 nm are associated with the $\pi-\pi^*$ transition of the phenolic chromophore.[28,45,46] The lowest energy absorption at 360–440 nm is assigned to a $\pi-\pi^*$ transition of the ligand framework with significant involvement of the π orbitals from the azomethine group.[46] Thus, this transition is expected to have the largest dependence on the size and charge of the coordinated metal center. $\mathbf{H_4L^{2+}}$, having the highest charge density in the ligand core, shows the lowest energy for this $\pi-\pi^*$ transition at 434 nm. The transition shifts to higher energy (380 nm) in both $\mathbf{Mn_2LAc^+}$ and $\mathbf{Zn_2LAc^+}$ as the metal centers have similar charge densities.

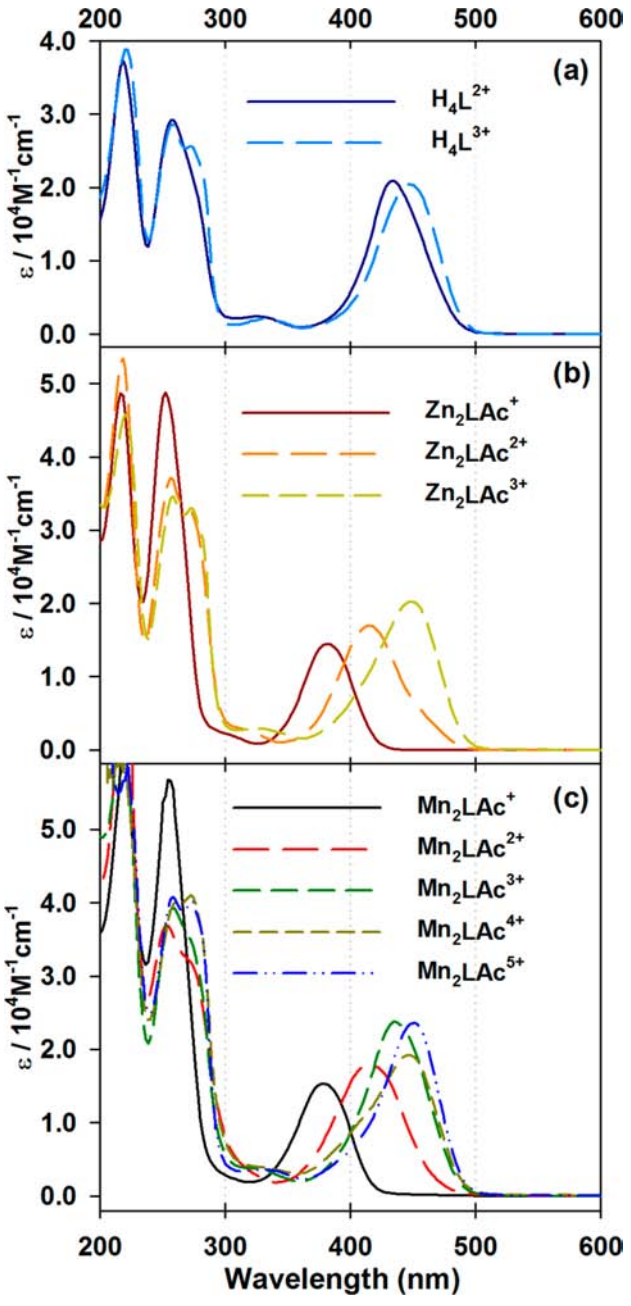

Figure 4. Comparison of UV–visible absorbance spectra of (a) $\mathbf{H_4L^{2+}}$, (b) $\mathbf{Zn_2LAc^+}$, and (c) $\mathbf{Mn_2LAc^+}$ in ACN at 0 °C and higher oxidation states generated by stoichiometric additions of $NOPF_6$.

The sizable difference in oxidation potentials from the electrochemistry measurements allows near quantitative isolation of the one-electron-oxidized intermediate steps for $\mathbf{Mn_2LAc^+}$, $\mathbf{Zn_2LAc^+}$, and $\mathbf{H_4L^{2+}}$. Included in Figure 4 are the electronic absorption spectra of higher oxidation states for these complexes obtained in anhydrous ACN at 0 °C with nitrosonium hexafluorophosphate ($NOPF_6$) as an oxidizing agent. Distinct isosbestic points were observed during the titrations with $NOPF_6$, indicating complete oxidation of the intermediates without any dissociation or decomposition (see Figures S4–S6 in the Supporting Information). The lack of new vibrational bands associated with Mn-NO in the IR spectra for $\mathbf{Mn_2LAc^+}$ suggests that acetate coordination was not effected during oxidation (vide infra). In addition, the lack of an absorption band at 352 nm for 4-*tert*-butyl-2,6-diformylphenol indicates the one-electron-oxidized intermediates are stable over the course of the experiment.[47]

Only one oxidative transformation was observed for $\mathbf{H_4L^{2+}}$ (see Figure 4a, as well as Figure S4 in the Supporting Information) with the addition of 1 equiv of NO^+, resulting in a red-shift of the band at 434 nm to 450 nm and a simultaneous appearance of a doublet at ~252–284 nm. We are unable to produce $\mathbf{H_4L^{4+}}$, suggesting the redox potential of NO^+ is not sufficient for further oxidation beyond $\mathbf{H_4L^{3+}}$. The ground-state absorbance spectrum of $\mathbf{Zn_2LAc^+}$ (Figure 4b) shows three transitions at 382, 252, and 217 nm. Spectrophotometric titration of $\mathbf{Zn_2LAc^+}$ with NO^+ produced two oxidative transitions at 1 and 2 equiv (see Figure S5 in the Supporting Information). The spectrum for $\mathbf{Zn_2LAc^{2+}}$ resulted in a red-shift of the absorbance band at 358 nm to 410 nm, a decrease in absorbance at 252 nm, and the appearance of a new shoulder in the absorbance band at 274 nm. Continued oxidation to $\mathbf{Zn_2LAc^{3+}}$ results in another red-shift of the lowest energy band from 410 nm to 450 nm and the appearance of a distinct doublet at 246 and 284 nm. Since the central Zn metals are redox inactive at these potentials, the new transitions are assigned to oxidations of the phenolate ligands.

Spectrophotometric titration of $\mathbf{Mn_2LAc^+}$ with NO^+ revealed four distinct redox transitions corresponding to the single electron oxidations of $\mathbf{Mn_2LAc^+}$ to $\mathbf{Mn_2LAc^{5+}}$ (see Figure 4c, as well as Figure S6 in the Supporting Information). Based on the electrochemical assignments above, the first two oxidations are associated with a red-shift of the absorbance band at 378 nm for $\mathbf{Mn^{II}_2LAc^+}$ to 416 nm for $\mathbf{Mn^{II}Mn^{III}LAc^{2+}}$ and at 430 nm for $\mathbf{Mn^{III}_2LAc^{3+}}$. The red-shift of this absorption band is consistent with the involvement of the π orbitals from the azomethine

dx.doi.org/10.1021/ic401631e | *Inorg. Chem.* 2013, 52, 13963–13973

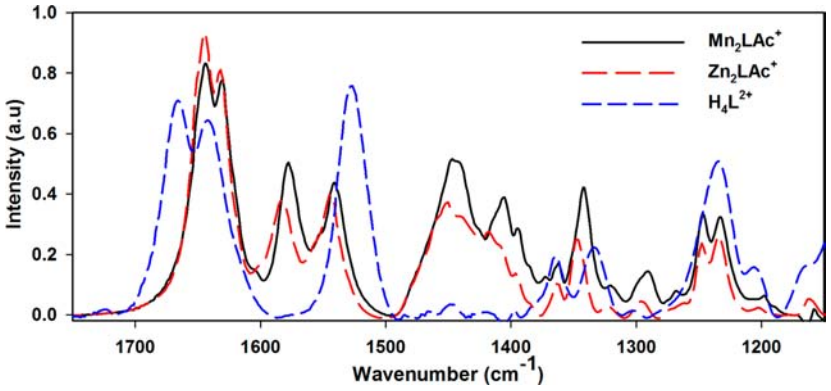

Figure 5. Comparison of FT-IR spectra of $\mathbf{Mn_2LAc^+}$ (black), $\mathbf{Zn_2LAc^+}$ (red), and $\mathbf{H_4L^{2+}}$ (blue) in a KBr pellet.

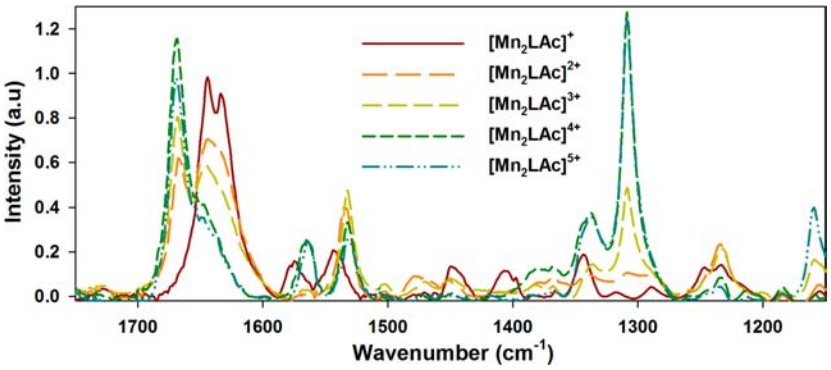

Figure 6. FT-IR spectral changes upon chemical oxidation of $\mathbf{Mn_2LAc^+}$ with stoichiometric additions of $NOPF_6$.

groups for this transition and the increasing positive charge of the metal centers.[46] Two additional absorbance transformations are observed upon the addition of 3 and 4 equiv of oxidant, corresponding to oxidation waves III and IV observed electrochemically (Figure 2b), resulting in a further red-shift of the lowest energy transition. In addition, a doublet at ~246–284 nm appears following these oxidations, similar to the initial oxidations of $\mathbf{Zn_2LAc^+}$ and $\mathbf{H_4L^{2+}}$. Given the striking similarities between the third and fourth spectral transitions of complex $\mathbf{Mn_2LAc^+}$ with that of the first two transitions for complex $\mathbf{Zn_2LAc^+}$, we can ascribe the later two transitions in $\mathbf{Mn_2LAc^+}$ resulting from the sequential oxidation of the phenolate moieties. During the course of this experiment, it has been observed that $\mathbf{Mn_2LAc^{2+}}$ and $\mathbf{Mn_2LAc^{3+}}$ are stable over a period of 5–6 h at room temperature, whereas the higher oxidation states corresponding to $\mathbf{Mn_2LAc^{4+}}$ and $\mathbf{Mn_2LAc^{5+}}$ are only stable over a period of an hour at 0 °C. Moreover, the chemical oxidations were found to be reversible using bis(cyclopentadineyl) cobalt(II) as the reducing agent, in anhydrous ACN at 0 °C (see Figure S7 in the Supporting Information).

Infrared Spectroscopy. Figure 5 displays the IR spectra of $\mathbf{Mn_2LAc^+}$, $\mathbf{Zn_2LAc^+}$, and $\mathbf{H_4L^{2+}}$ obtained in a KBr pellet and are consistent with the tetrakis-Schiff base macrocycles. All three show expected peaks for C═N (ν = 1641–1629 cm^{-1}), phenyl C–C (ν = 1539 cm^{-1}), and phenolic C–O stretch (ν = 1340 cm^{-1}).[12] In addition, $\mathbf{Mn_2LAc^+}$, and $\mathbf{Zn_2LAc^+}$ display peaks for the bridging acetate ligand at ν_{as} = 1577 cm^{-1} and ν_s = 1440 cm^{-1}. A difference of 137 cm^{-1} between the antisymmetric (ν_a) and symmetric stretching (ν_s) of the carboxylate is consistent with the bidentate bridging mode bonding of the acetate ion observed in the X-ray crystal structure.[48]

The higher oxidation states of $\mathbf{Mn_2LAc^+}$ were also examined in acetonitrile-d_3, using $NOPF_6$ as an oxidizing agent (Figure 6). The close match between the FT-IR spectra of $\mathbf{Mn_2LAc^+}$ in KBr disk and CD_3CN solution indicates the bridging acetate is not replaced by acetonitrile over the time scale of the experiment (hours). No additional vibrational bands were found for Mn–NO intermediates, suggesting that acetate coordination was not affected during oxidation. The structural changes at the central core of the tetrakis-Schiff base macrocycles for $\mathbf{Mn^{II}Mn^{III}LAc^{2+}}$ and $\mathbf{Mn^{III}_2LAc^{3+}}$ strongly influence the C═N and phenolic C–O stretching frequencies. As shown in Figure 6, the first two oxidations of $\mathbf{Mn_2LAc^+}$ are accompanied by a shift of the C═N stretch from 1641 cm^{-1} to 1668 cm^{-1} and disappearance of the doublet. As the central Mn(II) are oxidized to Mn(III), the stronger binding environment and decrease in Mn d-orbital backbonding induces a shift in the C═N stretch to higher energies. Oxidation to $\mathbf{Mn_2LAc^{4+}}$ and $\mathbf{MnLAc^{5+}}$ results in a shift and increase in the phenolic C–O stretch at ν = 1340 cm^{-1} to 1308 cm^{-1}.

Electronic Structure Calculations. Density functional theory electronic structure calculations were performed on $\mathbf{Zn_2LAc^+}$, $\mathbf{Mn_2LAc^+}$, $\mathbf{Mn_2LAc^{2+}}$, and $\mathbf{Mn_2LAc^{3+}}$ to predict the geometric structures of the various oxidation states where crystallographic information is not available. The structures were optimized using the B3LYP functional with the 6-311G(d,p) basis set for Zn, Mn, C, N, and H, and 6-311G(2df) for O. $\mathbf{Mn_2LAc^+}$, $\mathbf{Mn_2LAc^{2+}}$, and $\mathbf{Mn_2LAc^{3+}}$ were optimized using the broken symmetry (BS) formalism[49,50] to model the antiferromagnetic coupling between Mn centers.[13,18–23] The

dx.doi.org/10.1021/ic401631e | Inorg. Chem. 2013, 52, 13963–13973

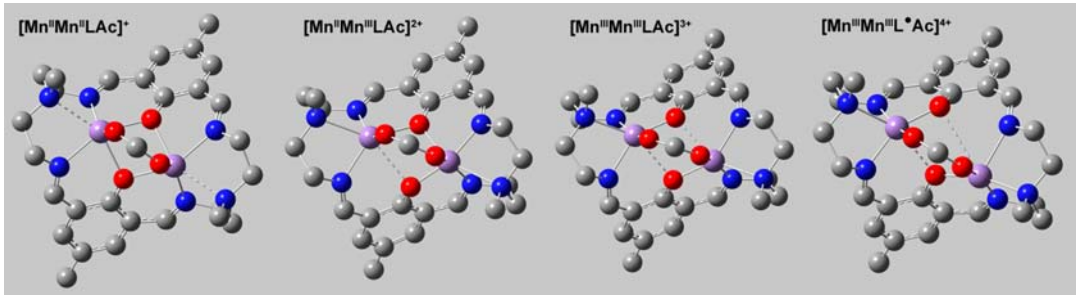

Figure 7. BS UB3LYP/6-311g(d,p)/6-311g(2df) geometry optimized structures for $\mathbf{Mn_2LAc^+}$, $\mathbf{Mn_2LAc^{2+}}$, $\mathbf{Mn_2LAc^{3+}}$, and $\mathbf{Mn_2LAc^{4+}}$. The dashed lines represent elongated bonds in the structure.

geometry optimized structures for $\mathbf{Mn_2LAc^+}$, $\mathbf{Mn_2LAc^{2+}}$, $\mathbf{Mn_2LAc^{3+}}$ and $\mathbf{Mn_2LAc^{4+}}$ are shown in Figure 7 and $\mathbf{Zn_2LAc^+}$ in Figure S8 in the Supporting Information. Relevant bond distances and angles are included with those obtained from crystallographic data in Table S1 in the Supporting Information. The B3LYP/6-311G(d,p)/6-311G(2df) level of theory is able to reproduce the crystallographically determined geometry of $\mathbf{Mn_2LAc^+}$ and $\mathbf{Zn_2LAc^+}$ quite well.

The calculated structure for $\mathbf{Mn^{II}Mn^{III}LAc^{2+}}$ shows a significant contraction of the coordination site around the Mn^{III} center, compared to that of $\mathbf{Mn^{II}_2LAc^+}$. In addition, there is an elongation of one of the Mn^{II}-phenolate bonds by 0.41 Å resulting in significant asymmetry of the di-Mn-phenoxo core. Further oxidation to $\mathbf{Mn^{III}_2LAc^{3+}}$ yields a contraction of the ligand around the second Mn^{III} center, but also an elongation of a Mn-phenolate bond. In $\mathbf{Mn^{III}_2LAc^{3+}}$, each Mn^{III} ion has one short (1.92 Å) and one long (2.47 Å) Mn-phenolate bond as expected for the Jahn−Teller distortion of the d^4 centers. The large structural changes observed computationally for the Mn_2-phenolate core throughout oxidation from $\mathbf{Mn^{II}_2LAc^+}$ to $\mathbf{Mn^{II}Mn^{III}LAc^{2+}}$ to $\mathbf{Mn^{III}_2LAc^{3+}}$ are consistent with the high reorganization and slow heterogeneous electron transfer rates measured electrochemically. The calculated structure for $\mathbf{Mn^{III}_2L^{\bullet}Ac^{4+}}$ reveals even more distortion in Mn_2-phenolate core with a significant elongation of one of the Mn−O bonds. The Mulliken spin populations (included in Table S2 in the Supporting Information) for $\mathbf{Mn_2LAc^+}$, $\mathbf{Mn_2LAc^{2+}}$, and $\mathbf{Mn_2LAc^{3+}}$ revealed that >99% of the spin density is localized on the two Mn centers, as expected for the metal-centered oxidations. Upon further oxidation to $\mathbf{Mn_2LAc^{4+}}$, the spin density remained roughly the same on the Mn centers, but increased significantly on the ligand framework, consistent with phenolate oxidation to the phenoxy radical.

In the calculated structures for $\mathbf{Mn_2LAc^+}$, $\mathbf{Mn_2LAc^{2+}}$, and $\mathbf{Mn_2LAc^{3+}}$ described above, the antiferromagnetically coupled low-spin state is favored by a small amount (92, 56, and 101 cm^{-1}, respectively), while in $\mathbf{Mn_2LAc^{4+}}$, it is somewhat higher (977 cm^{-1}) due to the strong coupling of the ligand radical to one of the Mn centers. The effective exchange parameter (J) for the magnetic interaction between Mn centers can be estimated from the DFT calculations, according to eq 2:

$$J = \frac{E^{HS} - E^{LS}}{\langle \hat{S}^2 \rangle^{LS} - \langle \hat{S}^2 \rangle^{HS}} \quad (2)$$

where E is the energy and $\langle \hat{S}^2 \rangle$ is the expectation value for the high-spin (HS) and low-spin (LS) states.[50,51] The estimated values of J were −3.7, −2.8, −6.3, and −48.5 cm^{-1} for $\mathbf{Mn_2LAc^+}$, $\mathbf{Mn_2LAc^{2+}}$, $\mathbf{Mn_2LAc^{3+}}$, and $\mathbf{Mn_2LAc^{4+}}$, respectively. The weak antiferromagnetic coupling calculated for $\mathbf{Mn_2LAc^+}$ is consistent with the room-temperature magnetic susceptibility measurement (7.76 μ_B) that is intermediate between the HS (S = 10/2) and LS (S = 0) states. Overall, the weak antiferromagnetic coupling of $\mathbf{Mn_2LAc^+}$, $\mathbf{Mn_2LAc^{2+}}$, and $\mathbf{Mn_2LAc^{3+}}$ are consistent with the low charge on the metal centers and the twisted geometry of the Mn-phenoxo core that places the orbitals of the phenolate oxygens out of plane with the coordinated Mn ions.[21]

Finally, time-dependent density functional theory (TD-DFT) calculations were performed on $\mathbf{Mn_2LAc^{n+}}$ (n = 1, 2, 3) in both the BS and HS configurations with the Polarizable Continuum Model (PCM) applied to include effects from the solvent (ACN). The resulting spectra are shown in Figure S9 in the Supporting Information and reveal a multitude of transitions in the UV-vis region. The spectra of $\mathbf{Mn_2LAc^+}$ is reasonably modeled with several intense transitions in the range of 375−425 nm that are primarily associated with the ligand framework, closely matching that observed experimentally. TD-DFT spectra for $\mathbf{Mn_2LAc^{2+}}$, and $\mathbf{Mn_2LAc^{3+}}$ show ligand-centered transitions that are red-shifted compared to $\mathbf{Mn_2LAc^+}$, but the relative intensities of the peaks are reduced significantly.

CONCLUSIONS

Incorporation of the 2,2′-diamino-*N*-methyldiethylamine backbone into a tetrakis-Schiff base macrocycle provides an N_6O_2 coordination environment for two transition-metal dications such as Mn^{2+} and Zn^{2+}. This ligand environment induces a highly distorted butterfly-like structure that presents two adjacent coordination sites on the metal centers that are bridged by acetate ions. Comparison of the electrochemical and spectroscopic properties of $\mathbf{Mn_2LAc^+}$, $\mathbf{Zn_2LAc^+}$, and $\mathbf{H_4L^{2+}}$ point to intricate electronic and structural changes involving both metal and ligand redox states. Electrochemical or chemical oxidation of $\mathbf{Zn_2LAc^+}$ and $\mathbf{H_4L^{2+}}$ are consistent with redox changes of the phenolate ligands. On the other hand, oxidation of $\mathbf{Mn_2LAc^+}$ first involves two Mn^{II} to Mn^{III} transitions before oxidation of the phenolate ligand framework. The sluggish interfacial electron transfer rates observed in electrochemical scans of $\mathbf{Mn_2LAc^+}$ are consistent with density functional theory (DFT) electronic structure calculations that predict a large structural rearrangement of the Mn coordination environment upon oxidation to Mn^{III} with associated Jahn−Teller distortions. To the best of our knowledge, this is the first thorough spectroscopic characterization of chemically generated higher oxidation states, correlated with electrochemical data, of di-Mn and Zn tetrakis-Schiff base macrocycles. This information will aid in future mechanistic studies of electro-

dx.doi.org/10.1021/ic401631e | *Inorg. Chem.* 2013, 52, 13963−13973

catalytic processes involving these and related dinuclear complexes.

EXPERIMENTAL SECTION

General Methods. NMR spectra were obtained on a Varian 500 MHz spectrometer, and the chemical shifts were referenced to the standard solvent shift. MALDI-TOF MS were obtained on a Bruker Ultraflex III. ESI MS were obtained on a Thermo Electron Finnigan TSQ Quantum Ultra. Elemental analysis were obtained from Atlantic Microlabs, Inc. (Norcross, GA). Electronic absorption spectra were taken on a Perkin−Elmer Lambda 950 or Agilent 8453A spectrophotometer at 0 °C with a 1.0 cm quartz cell under a nitrogen atmosphere.

Materials. 4-*tert*-Butyl-2,6-diformylphenol was purchased from Sigma−Aldrich and was purified by column chromatography on silica gel, eluting with dichloromethane. 2,2′-diamino-*N*-methyldiethylamine was purchased from TCI and used as received. All other chemicals and solvents employed in this work were of the highest purity available from Aldrich and Fluka. Anhydrous acetonitrile and dicholoromethane were purified by recirculating the nitrogen-purged solvent through a solid-state column purification system (Vacuum Atmospheres Company, Hawthorne, CA) prior to use.[52] Tetrabutylammonium hexafluorophosphate ($TBAPF_6$, Acros) was recrystallized twice from hot ethanol before use in electrochemical experiments.

$[Mn_2LAc](ClO_4)$. $Mn(ClO_4)_2{\cdot}6H_2O$ (200 mg, 0.55 mmol), 4-*tert*-butyl-2,6-diformylphenol (100 mg, 0.48 mmol) and sodium acetate (97 mg, 1.18 mmol) were dissolved in 10 mL of methanol and purged with nitrogen. *N*′-methyl-2,2′-diaminodiethyldiamine (62 μL, 0.48 mmol) was added to this solution, dissolved in 1 mL of methanol, added dropwise while stirring. The mixture was refluxed for 1.5 h under nitrogen, then cooled and the volume of the solvent reduced under reduced pressure to ∼2−3 mL. The resulting solution was kept at 0 °C for 24 h which yielded the yellow crystalline product. This was filtered and washed with cold methanol followed by anhydrous diethyl ether to obtain $[Mn_2LAc](ClO_4)$ (mass 157 mg, 70% yield).

[***Caution:*** *Perchlorate salts of metal complexes with organic ligands are potentially explosive. Only small quantities of these compounds should be prepared and handled behind a suitable protective shield.*] MALDI MS: m/z = 741.1 $[M-ClO_4]^+$. ESI MS: m/z = 741.3 $[M-ClO_4]^+$. Anal. Calcd. for $C_{36}H_{51}N_6O_8Mn_2Cl(H_2O)$: C, 50.33; H, 6.21; N, 9.78; Found: C, 50.45; H, 6.16; N, 9.77.

$[Zn_2LCl](PF_6)$. $ZnCl_2$ (40 mg, 0.29 mmol), 4-*tert*-butyl-2,6-diformylphenol (56 mg, 0.27 mmol), and triethylamine (38 μL, 0.27 mmol) were dissolved in 10 mL of ethanol and degassed with nitrogen. *N*′-methyl-2,2′-diaminodiethyldiamine (35 μL, 0.27 mmol) was added to this solution, in 1 mL of methanol, added dropwise while stirring. The mixture was refluxed for 1 h and tetrabutylammonium hexafluorophosphate (78 mg, 0.2 mmol) was added. This mixture was then stirred for an additional 30 min. Upon cooling, a pale-yellow precipitate formed, which was filtered and washed with cold methanol and anhydrous ether. The precipitate was recrystallizing from DCM by addition of diethyl ether to obtain $[Zn_2LCl](PF_6)$ (101 mg, 77% yield). MALDI MS: m/z = 735.1 $[M-PF_6]^+$. ^1H NMR (500 MHz, DMSO, 25 °C) δ 8.57 (s, 4H, HC═N), 7.58 (s, 4H, ArH), 3.58 (broad s, 8H, N−CH_2−CH_2−NCH_3), 2.75 (broad s, 8H, N−CH_2−CH_2−NCH_3), 2.35 (s, 6H, NCH_3), 1.27 (s, 18H, *t*-butyl).

$[Zn_2LAc](PF_6)$. $[Zn_2LCl](PF_6)$. (30.0 mg, 0.034 mmol) was dissolved in 10 mL of a 3:1 acetonitrile−methanol mixture. Sodium acetate (4.0 mg, 0.041 mmol) was added to this solution in 1 mL of methanol and stirred for 20 h under nitrogen. The solvent was removed under reduced pressure and the solid was extracted with DCM, filtered to remove the NaCl byproduct, and layered with hexanes to obtain a light yellow precipitate of $[Zn_2LAc](PF_6)$ (21 mg, 70% yield). MALDI MS: m/z = 759.2 $[M-PF_6]^+$. ^1H NMR (500 MHz, DMSO, 25 °C) δ 8.53 (s, 4H, HC═N), 7.53 (s, 4H, ArH), 3.73 (s, 4H, N−CH_2−CH_2−NCH_3), 3.49 (m, 4H, N−CH_2−CH_2−NCH_3), 2.84 (q, 8H, N−CH_2−CH_2−NCH_3), 2.39 (s, 6H, NCH_3), 1.94 (s, 3, CH_3COO), 1.25 (s, 18H, *t*-butyl). Anal. Calcd. for $C_{36}H_{51}N_6O_4Zn_2PF_6$: C, 47.64; H, 5.66; N, 9.26; Found: C, 47.70; H, 5.57; N, 9.41.

$[H_4L](ClO_4)_2$. 4-*tert*-Butyl-2,6-diformylphenol (100 mg, 0.48 mmol) and sodium perchlorate (539 mg, 4.4 mmol) were dissolved in 10 mL of methanol and degassed with nitrogen. Acetic acid (69 μL, 1.2 mmol) was added with stirring. *N*′-methyl-2,2′-diaminodiethyldiamine (62 μL, 0.48 mmol) was added to this solution, in 1 mL of methanol, added dropwise under nitrogen, and the mixture was refluxed for 3 h. After cooling, the solution was concentrated under reduced pressure and kept overnight at 0 °C. The product separated as a dark orange precipitate and was collected by filtration and washed with cold ethanol and anhydrous ether (107 mg, 57.7%). MALDI MS: m/z = 575.3 $[M-H^+-2ClO_4]^+$. ^1H NMR (500 MHz, CD_3CN, 25 °C) δ 13.26 (broad s, 4H), 8.19 (s, 4H, HC═N), 7.52 (s, 4H, ArH), 3.80 (s, 8H, N-CH_2−CH_2−NCH_3), 2.92 (s, 8H, N−CH_2−CH_2−NCH_3), 2.46 (s, 6H, NCH_3), 1.17 (s, 18H, *t*-butyl). Anal. Calcd. for $C_{34}H_{55}N_6O_{15}Cl_3$: C, 45.72; H, 6.09; N, 9.41. Found: C, 46.66; H, 5.99; N, 9.60.

Crystal Structure Determinations and Refinement. Crystals of $[Mn_2LAc](ClO_4)$ suitable for X-ray crystallography were obtained via two different methods. One batch was obtained by slow diffusion of diethyl ether into a $[Mn_2LAc](ClO_4)$ solution of dimethyl formamide, and the second set was grown by slow diffusion of diethyl ether into a methanol−acetonitrile solution of $[Mn_2LAc](ClO_4)$. Crystals of $[Zn_2LCl](PF_6)$ suitable for X-ray crystallography were obtained by slow diffusion of ether into a dimethylformamide saturated solution. Data collection was performed on a Bruker SMART APEX CCD-based X-ray diffractometer with graphite-monochromated Mo Kα radiation (λ = 0.71073 Å) at T = 100(2) K. The frames were integrated with the Bruker SAINT software package[53] and data were corrected for absorption effects using the empirical method SADABS.[54] The structure was solved by direct methods and refined using the Bruker SHELXTL software package.[55,56] H atoms were included at idealized positions using the riding model. Crystal data for $[Mn_2LAc](ClO_4)$ and $[Zn_2LCl](PF_6)$ are shown in Table 1. In both structures of $[Mn_2LAc](ClO_4)$, there is disorder in the position of the ClO_4^- counterion and solvent of crystallization. Moreover, there is some disorder in the *tert*-butyl groups and *N*′-methyl-2,2′-diaminodiethyldiamine backbone on one-half of the molecule. All disorders in these structures were individually modeled where necessary.

Magnetic Susceptibility. The magnetic susceptibility of $[Mn_2LAc](ClO_4)$ was measured on a Johnson Matthey (Mark1) magnetic susceptibility meter by Gouy's method at room temperature (298 K) and corrected for diamagnetic contributions using Pascal's constants.

Electrochemistry. All cyclic voltammetric experiments were performed and analyzed using a Model CHI440A (CH Instruments, Austin, TX) potentiostat. Electrolyte solutions (0.1 M tetrabutylammonium hexafluorophosphate ($TBAPF_6$)) were prepared with anhydrous solvents and deoxygenated with nitrogen prior to use. A Pt wire was used as the counter electrode and a glassy carbon macrodisk electrode was used as the working electrode. A silver wire was used as a pseudoreference electrode with ferrocene (purified by sublimation) added as an internal reference at the end of each experiment. All experiments were run under a nitrogen atmosphere. DPV scans utilized the following: step potential, 4 mV; amplitude, 50 mV; pulse width, 100 ms; and pulse period, 300 ms. Digital simulations of the cyclic voltammograms for Mn_2LAc^+ were performed using the software associated with the CH Instruments Model CHI440A potentiostat using the experimentally derived diffusion coefficient.

Computational Details. Electronic structure calculations were conducted using the Blacklight supercomputing resource, which is part of the facilities of the National Science Foundation Teragrid Computing System at the Pittsburgh Supercomputer Center. Geometry optimizations for Mn_2LAc^{n+} (n = 1, 2, 3, 4) and Zn_2LAc^+ were carried out using density functional theory (DFT), as implemented in Gaussian 09, Revision C.01.[57] Initial geometries were taken from X-ray crystal structures and the *tert*-butyl groups were

dx.doi.org/10.1021/ic401631e | *Inorg. Chem.* 2013, 52, 13963−13973

replaced with methyls to reduce computational time. Becke's three-parameter hybrid functional[58−61] with the LYP correlation functional[62] (B3LYP) was used with the 6-311G(2df) basis sets for O, and the 6-311G(d) basis sets for Mn, Zn, C, N, and H. For $\mathbf{Mn_2LAc}^{n+}$ (n = 1, 2, 3, and 4), the initial geometry optimizations were performed in the gas phase for the high-spin state (ferromagnetic interactions between Mn ions), and the low energy conformations were confirmed by frequency analysis. The geometries were further optimized in the broken symmetry formalism[49,50] using the fragment option in Gaussian 09 to model the antiferromagnetic coupling between Mn ions.[18,19] Table S3 in the Supporting Information contains Cartesian coordinates and ZPE corrected total energies of the optimized structures. Finally, the lowest 100 electronic states were predicted by TD-DFT with the Polarizable Continuum Model (PCM) applied to include effects from the solvent (acetonitrile).

■ ASSOCIATED CONTENT

Ⓢ Supporting Information

Crystallographic data in CIF format; ORTEP diagram for $[Mn_2LAc](ClO_4)\cdot(ACN)_{0.5}$; digital simulation of CVs of $\mathbf{Mn_2LAc}^{+}$; spectrophotometric titrations of $\mathbf{H_4L}^{2+}$, $\mathbf{Zn_2LAc}^{+}$, and $\mathbf{Mn_2LAc}^{+}$ with $NOPF_6$ and cobaltocene; DFT geometry optimized structure of $\mathbf{Zn2LAc}^{+}$; DFT energies and Mulliken spin populations for $\mathbf{Mn_2LAc}^{n+}$ (n = 1, 2, 3, and 4); and Cartesian coordinates of the DFT optimized structures. This material is available free of charge via the Internet at http://pubs.acs.org.

■ AUTHOR INFORMATION

Corresponding Author

*E-mail: dinolp@rpi.edu.

Notes

The authors declare no competing financial interest.

■ ACKNOWLEDGMENTS

This work was supported in part by Rensselaer Polytechnic Institute and the New York State Energy Research and Development Authority (Award No. 30940). S.K. acknowledges a Slezak Memorial Fellowship. Computation aspects of this work used the Blacklight system at the Pittsburgh Supercomputing Center (Allocation Nos. TG-CHE130030 and TG-CHE130109) as part of the Extreme Science and Engineering Discovery Environment (XSEDE), which is supported by National Science Foundation (Grant No. OCI-1053575).

■ REFERENCES

(1) Mukhopadhyay, S.; Mandal, S. K.; Bhaduri, S.; Armstrong, W. H. *Chem. Rev.* **2004**, *104*, 3981−4026.
(2) Wu, A. J.; Penner-Hahn, J. E.; Pecoraro, V. L. *Chem. Rev.* **2004**, *104*, 903−938.
(3) Tagore, R.; Crabtree, R. H.; Brudvig, G. W. *Inorg. Chem.* **2008**, *47*, 1815−1823.
(4) Manchanda, R.; Brudvig, G. W.; Crabtree, R. H. *Coord. Chem. Rev.* **1995**, *144*, 1−38.
(5) Ōkawa, H.; Furutachi, H.; Fenton, D. E. *Coord. Chem. Rev.* **1998**, *174*, 51−75.
(6) Gavrilova, A. L.; Bosnich, B. *Chem. Rev.* **2004**, *104*, 349−384.
(7) Vigato, P. A.; Tamburini, S.; Bertolo, L. *Coord. Chem. Rev.* **2007**, *251*, 1311−1492.
(8) Vigato, P. A.; Tamburini, S. *Coord. Chem. Rev.* **2004**, *248*, 1717−2128.
(9) Atkins, A. J.; Black, D.; Blake, A. J.; Marin-Becerra, A.; Parsons, S.; Ruiz-Ramirez, L.; Schroder, M. *Chem. Commun.* **1996**, 457−464.
(10) Zanello, P.; Tamburini, S.; Vigato, P. A.; Mazzocchin, G. A. *Coord. Chem. Rev.* **1987**, *77*, 165−273.
(11) Robson, R. *Aust. J. Chem.* **1970**, *23*, 2217−2224.
(12) Pilkington, N. H.; Robson, R. *Aust. J. Chem.* **1970**, *23*, 2225−2236.
(13) Chang, H.-R.; Larsen, S. K.; Boyd, P. D. W.; Pierpont, C. G.; Hendrickson, D. N. *J. Am. Chem. Soc.* **1988**, *110*, 4565−4576.
(14) Jana, A.; Aliaga-Alcalde, N.; Ruiz, E.; Mohanta, S. *Inorg. Chem.* **2013**, *52*, 7732−7746.
(15) Ikawa, Y.; Nagata, T.; Maruyama, K. *Chem. Lett.* **1993**, *22*, 1049−1052.
(16) Nagata, T.; Ikawa, Y.; Maruyama, K. *J. Chem. Soc., Chem. Commun.* **1994**, 471−472.
(17) Nagata, T.; Mizukami, J. *J. Chem. Soc., Dalton Trans.* **1995**, 2825−2830.
(18) Qian, M.; Gou, S.; Chantrapromma, S.; Sundara, R. S. S.; Fun, H. K.; Zeng, Q.; Yu, Z.; You, X. *Inorg. Chim. Acta* **2000**, *305*, 83−90.
(19) Qian, M.; Gou, S.; Yu, Z.; Ju, H.; Xu, Y.; Duan, C.; You, X. *Inorg. Chim. Acta* **2001**, *317*, 157−162.
(20) Downard, A. J.; McKee, V.; Tandon, S. S. *Inorg. Chim. Acta* **1990**, *173*, 181−190.
(21) Lambert, S. L.; Hendrickson, D. N. *Inorg. Chem.* **1979**, *18*, 2683−2686.
(22) Timken, M. D.; Marritt, W. A.; Hendrickson, D. N.; Gagne, R. A.; Sinn, E. *Inorg. Chem.* **1985**, *24*, 4202−4208.
(23) Aono, T.; Wada, H.; Yonemura, M.; Ohba, M.; Okawa, H.; E. Fenton, D. *J. Chem. Soc., Dalton Trans.* **1997**, 1527−1532.
(24) Jiang, J.-C.; Chu, Z.-L.; Huang, W.; Wang, G.; You, X.-Z. *Inorg. Chem.* **2010**, *49*, 5897−5911.
(25) Dutta, B.; Bag, P.; Adhikary, B.; Flörke, U.; Nag, K. *J. Org. Chem.* **2004**, *69*, 5419−5427.
(26) Wada, H.; Motoda, K.-i.; Ohba, M.; Sakiyama, H.; Matsumoto, N.; Okawa, H. *Bull. Chem. Soc. Jpn.* **1995**, *68*, 1105−1114.
(27) Diril, H.; Chang, H.-R.; Zhang, X.; Larsen, S. K.; Potenza, J. A.; Pierpont, C. G.; Schugar, H. J.; Isied, S. S.; Hendrickson, D. N. *J. Am. Chem. Soc.* **1987**, *109*, 6207−6208.
(28) Soler, M.; McCusker, J. K. *J. Am. Chem. Soc.* **2008**, *130*, 4708−4724.
(29) Luo, Y.; Zhang, J.; Lu, L.; Qian, M.; Wang, X.; Yang, X.; Jian, F. *Transition Met. Chem. (Dordrecht, Neth.)* **2002**, *27*, 469−472.
(30) Müller, J.; Kikuchi, A.; Bill, E.; Weyhermüller, T.; Hildebrandt, P.; Ould-Moussa, L.; Wieghardt, K. *Inorg. Chim. Acta* **2000**, *297*, 265−277.
(31) Kurahashi, T.; Fujii, H. *J. Am. Chem. Soc.* **2011**, *133*, 8307−8316.
(32) Goldberg, D. P.; Koulougliotis, D.; Brudvig, G. W.; Lippard, S. J. *J. Am. Chem. Soc.* **1995**, *117*, 3134−3144.
(33) Chaudhuri, P.; Wieghardt, K. In *Progress in Inorganic Chemistry*, Vol. *50*; John Wiley & Sons, Inc.: Hoboken, NJ, 2002; pp 151−216.
(34) Kurahashi, T.; Kikuchi, A.; Tosha, T.; Shiro, Y.; Kitagawa, T.; Fujii, H. *Inorg. Chem.* **2008**, *47*, 1674−1686.
(35) Bill, E.; Müller, J.; Weyhermüller, T.; Wieghardt, K. *Inorg. Chem.* **1999**, *38*, 5795−5802.
(36) Sokolowski, A.; Müller, J.; Weyhermüller, T.; Schnepf, R.; Hildebrandt, P.; Hildenbrand, K.; Bothe, E.; Wieghardt, K. *J. Am. Chem. Soc.* **1997**, *119*, 8889−8900.
(37) Baranski, A. S.; Fawcett, W. R.; Gilbert, C. M. *Anal. Chem.* **1985**, *57*, 166−170.
(38) Richardson, D. E.; Taube, H. *Inorg. Chem.* **1981**, *20*, 1278−1285.
(39) Ward, M. D. *Chem. Soc. Rev.* **1995**, *24*, 121−134.
(40) Kalyanasundaram, K.; Nazeeruddin, M. K. *Inorg. Chim. Acta* **1994**, *226*, 213−230.
(41) Giuffrida, G.; Campagna, S. *Coord. Chem. Rev.* **1994**, *135−136*, 517−531.
(42) Creutz, C. In *Progress in Inorganic Chemistry: An Appreciation of Henry Taube*, Vol. *30*; John Wiley & Sons, Inc.: Hoboken, NJ, 2007; pp 1−73.

(43) Bard, A. J.; Faulkner, L. R. In *Electrochemical Methods: Fundamentals and Applications*, 2nd Edition; Wiley: New York, 2001.
(44) Anderlund, M. F.; Högblom, J.; Shi, W.; Huang, P.; Eriksson, L.; Weihe, H.; Styring, S.; Åkermark, B.; Lomoth, R.; Magnuson, A. *Eur. J. Inorg. Chem.* **2006**, *2006*, 5033−5047.
(45) Cook, C. D.; Woodworth, R. C. *J. Am. Chem. Soc.* **1953**, *75*, 6242−6244.
(46) Bosnich, B. *J. Am. Chem. Soc.* **1968**, *90*, 627−632.
(47) Mitra, S.; Das, R.; Guha, D.; Mukherjee, S. *Spectrochim. Acta. A* **1998**, *54*, 1073−1081.
(48) Tackett, J. E. *Appl. Spectrosc.* **1989**, *43*, 483−489.
(49) Norman, J. G.; Ryan, P. B.; Noodleman, L. *J. Am. Chem. Soc.* **1980**, *102*, 4279−4282.
(50) Noodleman, L. *J. Chem. Phys.* **1981**, *74*, 5737−5743.
(51) Soda, T.; Kitagawa, Y.; Onishi, T.; Takano, Y.; Shigeta, Y.; Nagao, H.; Yoshioka, Y.; Yamaguchi, K. *Chem. Phys. Lett.* **2000**, *319*, 223−230.
(52) Pangborn, A. B.; Giardello, M. A.; Grubbs, R. H.; Rosen, R. K.; Timmers, F. J. *Organometallics* **1996**, *15*, 1518−1520.
(53) *SAINT, Version 6.02*; Bruker AXS, Inc.: Madison, WI, 2001.
(54) *SADABS*; Bruker AXS, Inc.: Madison, WI, 2001.
(55) *SHELXTL Version 6.14*; Bruker AXS: Madison, WI, 2000.
(56) Sheldrick, G. *Acta Crystallogr., Sect. A* **2008**, *64*, 112−122.
(57) Frisch, M. J.; Trucks, G. W.; Schlegel, H. B.; Scuseria, G. E.; Robb, M. A.; Cheeseman, J. R.; Scalmani, G.; Barone, V.; Mennucci, B.; Petersson, G. A.; Nakatsuji, H.; Caricato, M.; Li, X.; Hratchian, H. P.; Izmaylov, A. F.; Bloino, J.; Zheng, G.; Sonnenberg, J. L.; Hada, M.; Ehara, M.; Toyota, K.; Fukuda, R.; Hasegawa, J.; Ishida, M.; Nakajima, T.; Honda, Y.; Kitao, O.; Nakai, H.; Vreven, T.; Montgomery, J. A., Jr.; Peralta, J. E.; Ogliaro, F.; Bearpark, M.; Heyd, J. J.; Brothers, E.; Kudin, K. N.; Staroverov, V. N.; Keith, T.; Kobayashi, R.; Normand, J.; Raghavachari, K.; Rendell, A.; Burant, J. C.; Iyengar, S. S.; Tomasi, J.; Cossi, M.; Rega, N.; Millam, J. M.; Klene, M.; Knox, J. E.; Cross, J. B.; Bakken, V.; Adamo, C.; Jaramillo, J.; Gomperts, R.; Stratmann, R. E.; Yazyev, O.; Austin, A. J.; Cammi, R.; Pomelli, C.; Ochterski, J. W.; Martin, R. L.; Morokuma, K.; Zakrzewski, V. G.; Voth, G. A.; Salvador, P.; Dannenberg, J. J.; Dapprich, S.; Daniels, A. D.; Farkas, O.; Foresman, J. B.; Ortiz, J. V.; Cioslowski, J.; Fox, D. J. *Gaussian 09, Revision D.01*, Gaussian, Inc., Wallingford, CT, 2010.
(58) Becke, A. D. *Phys. Rev. A* **1988**, *38*, 3098−3100.
(59) Becke, A. D. *J. Chem. Phys.* **1993**, *98*, 1372−1377.
(60) Becke, A. D. *J. Chem. Phys.* **1993**, *98*, 5648−5652.
(61) Stephens, P. J.; Devlin, F. J.; Chabalowski, C. F.; Frisch, M. J. *J. Phys. Chem.* **1994**, *98*, 11623−11627.
(62) Lee, C.; Yang, W.; Parr, R. G. *Phys. Rev. B* **1988**, *37*, 785−789.